INTERNATIONAL JOURNAL FOR NUMERICAL METHODS IN FLUIDS
Int. J. Numer. Meth. Fluids 2002; **38**:99–123 (DOI: 10.1002/fld.204)

A 3D incompressible Navier–Stokes velocity–vorticity weak form finite element algorithm

K. L. Wong[1,*] and A. J. Baker[2]

[1] *The Joint Institute for Computational Science, The University of Tennessee, Knoxville, TN 37996, U.S.A.*
[2] *Department of Mechanical & Aerospace Engineering and Engineering Science, The University of Tennessee, Knoxville, TN 37996, U.S.A.*

SUMMARY

The velocity–vorticity formulation is selected to develop a time-accurate CFD finite element algorithm for the incompressible Navier–Stokes equations in three dimensions. The finite element implementation uses equal order trilinear finite elements on a non-staggered hexahedral mesh. A second order vorticity kinematic boundary condition is derived for the no slip wall boundary condition which also enforces the incompressibility constraint. A biconjugate gradient stabilized (BiCGSTAB) sparse iterative solver is utilized to solve the fully coupled system of equations as a Newton algorithm. The solver yields an efficient parallel solution algorithm on distributed-memory machines, such as the IBM SP2. Three dimensional laminar flow solutions for a square channel, a lid-driven cavity, and a thermal cavity are established and compared with available benchmark solutions. Copyright © 2002 John Wiley & Sons, Ltd.

KEY WORDS: finite element algorithms; incompressible Navier–Stokes equations; velocity–vorticity formulation

1. INTRODUCTION

In the last decade, developments and advancement in computer technology, especially the availability of the massively parallel machines, have escalated the numerical treatment of complex fluid flow problems to a new height. Numerical simulation of incompressible viscous fluid flow, often associated with practical industrial and environmental applications, is receiving intense scrutiny to perform in the promising distributed parallel computing environment. On the other hand, the field of computational fluid dynamics continues to explore and exploit unified and geometrically versatile formulations in contention with the notorious divergence-free velocity field constraint, for the incompressible Navier–Stokes equations in three dimensions. The velocity–vorticity formulation is chosen with the full intent to resolve these issues.

* Correspondence to: K. L. Wong, The Joint Institute for Computational Science, The University of Tennessee, Knoxville, TN 37996, U.S.A.

Received 31 January 2001
Revised 15 March 2001

Many different finite element algorithms have been introduced in the last decade to predict viscous incompressible flows. They may be classified into two major categories: primitive (velocity-pressure) variable formulations, and derived variable (vorticity) formulations. For the former, Gresho and Sani [1] point out that the pressure appearing in the incompressible Navier–Stokes (INS) equations is not a thermodynamic variable. Instead, it functions mathematically as a Lagrangian constraint that instantaneously enforces conservation of mass via a divergence-free velocity field throughout the entire flow field at any time. The primary challenge in all primitive variable INS formulations is to satisfy the continuity equation, $\nabla \cdot \mathbf{u} = 0$, contending with how the pressure variable works in a CFD theory, or working around it. In sharp distinction, by using the definition of vorticity, the continuity equation, and the curl of the momentum equations, the INS equations can be written exclusively in terms of velocity and vorticity. The isothermal formulation consists of three velocity Poisson equations and three vorticity transport equations. The thermal form appends the temperature transport equations.

There are several distinct advantages to using the velocity–vorticity formulation for the INS equations. First, pressure does not explicitly appear in the field equations, thus difficulties associated with the determination of the pressure boundary conditions, especially at the outflow boundary [2], are avoided. Second, the boundary conditions for the formulation are clearer and easier to impose than streamvector or vector-potential formulations. Third, it can predict time-accurate incompressible flows in three dimensions.

The velocity–vorticity CFD formulation was first reported by Fasel [3] to study the stability of boundary layers in two dimensions. When the velocity–vorticity formulation is written using a standard finite difference construction, a staggered grid spatial discretization is employed to satisfy the continuity constraint. Using this arrangement, Orlandi [4] obtained a solution for flow over a two dimensional backward facing step using a block ADI method. Steady state solutions for two dimensional driven cavity flows at $Re \leqslant 5000$, were reported by Guj and Stella [5] using the false transient method. Solutions for an axisymmetric flow in a closed cylinder was also reported by Daube [6] using the influence matrix technique. Solutions for the three dimensional driven cavity benchmark using a finite difference method in conjunction with a staggered grid arrangement were reported by Dacles and Hafez [7] and Napolitano and Pascazio [8].

Two dimensional viscous flow solutions using the finite element method for velocity–vorticity form were first reported by Guevremont *et al.* [9]. Their methods utilized quadratic finite elements for the velocity components and linear for the vorticity. The vorticity boundary condition at a no-slip wall was imposed by evaluating the weighted area integral of the kinematic definition of vorticity in terms of velocity in each boundary element. Three dimensional viscous flow solutions for driven cavity flow at $Re = 100$ and $Re = 400$ were also reported [10].

As mathematically viable as the velocity–vorticity formulation appears, constructing a robust three dimensional algorithm is a challenge. The isothermal formulation contains six variables. The system of algebraic equations must be solved fully coupled to guarantee a solenoidal velocity field. Solving such a fully coupled implicit system on a sequential machine would be prohibitively expensive. Hence, an efficient parallel numerical algebra procedure represents an important issue to be resolved. It is these challenges that motivate this investigation of a new, time accurate, parallel finite element algorithm for the 3D unsteady incompressible Navier–Stokes equations in velocity–vorticity form.

The developed finite element methodology uses equal order trilinear finite elements for both velocity and vorticity components on a non-staggered hexahedral mesh. A second order kinematic vorticity boundary condition is derived and shown to enforce the incompressibility constraint. The biconjugate gradient stabilized (BiCGSTAB) [11] sparse iterative solver is used for the terminal fully coupled matrix statement, which can be effectively implemented on any distributed-memory parallel machine.

This paper derives the formulation and presents the parallel implementation of the implicit finite element algorithm. Three dimensional laminar flow solutions of a square channel, a lid-driven cavity, and a thermal cavity are computed and compared with available benchmark solutions.

2. VELOCITY–VORTICITY INS FORMULATION

2.1. Governing equations

The nondimensional, laminar flow incompressible Navier–Stokes equation system with Boussinesq body-force approximation is,

Continuity:

$$\nabla \cdot \mathbf{u} = 0 \tag{1}$$

Momentum:

$$\frac{\partial \mathbf{u}}{\partial t} + (\mathbf{u} \cdot \nabla)\mathbf{u} = -\nabla P + \frac{1}{Re}\nabla^2 \mathbf{u} - \frac{Gr}{Re^2}\Theta \hat{g} \tag{2}$$

Energy:

$$\frac{\partial \Theta}{\partial t} + (\mathbf{u} \cdot \nabla)\Theta = \frac{1}{RePr}\nabla^2 \Theta \tag{3}$$

where $\mathbf{u} = \mathbf{u}(\mathbf{x}, t) = (u, v, w)$ is the velocity vector field, t is the time, $\mathbf{x} = (x, y, z)$ is the spatial coordinate, Θ is the potential temperature, $\hat{\mathbf{g}}$ is the gravity unit vector and P is the kinematic pressure. The nondimensional parameters are Reynolds number (Re), Prandtl number (Pr), and Grashof number (Gr) defined as,

$$Re = \frac{U_r L_r}{\nu}, \quad Pr = \frac{\nu}{\alpha}, \quad Gr = \frac{\beta g \Delta T_r L_r^3}{\nu^2}$$

where L_r and U_r are the reference length and velocity respectively, g is the gravity acceleration, ν is the kinematic viscosity, β is the coefficient of volume expansion, α is the thermal diffusivity, and ΔT_r is the reference temperature difference.

The vorticity vector, $\mathbf{\Omega} = (\Omega_x, \Omega_y, \Omega_z)$, is kinematically defined as

$$\mathbf{\Omega} = \nabla \times \mathbf{u} \tag{4}$$

Taking the curl of definition (4), together with the incompressibility constraint (1) and the vector identity,

$$\nabla \times \mathbf{\Omega} = \nabla \times \nabla \times \mathbf{u} = \nabla(\nabla \cdot \mathbf{u}) - \nabla^2 \mathbf{u} \tag{5}$$

yields the velocity vector Poisson equation system

$$\nabla^2\mathbf{u} = -\nabla\times\boldsymbol{\Omega} \tag{6}$$

Taking the curl of the momentum Equation (2) eliminates any gradient field. Applying Equation (1) and noting $\nabla\cdot\boldsymbol{\Omega}=0$, the vorticity transport equation is

$$\frac{\partial\boldsymbol{\Omega}}{\partial t} + (\mathbf{u}\cdot\nabla)\boldsymbol{\Omega} - (\boldsymbol{\Omega}\cdot\nabla)\mathbf{u} = \frac{1}{Re}\nabla^2\boldsymbol{\Omega} - \frac{Gr}{Re^2}\nabla\times\Theta\hat{\mathbf{g}} \tag{7}$$

Hence, the velocity–vorticity formulation for the laminar INS equations system with Boussinesq approximation in three dimensions can be written as

$$\nabla^2\mathbf{u} + \nabla\times\boldsymbol{\Omega} = 0 \tag{8}$$

$$\frac{\partial\boldsymbol{\Omega}}{\partial t} + (\mathbf{u}\cdot\nabla)\boldsymbol{\Omega} - (\boldsymbol{\Omega}\cdot\nabla)\mathbf{u} - \frac{1}{Re}\nabla^2\boldsymbol{\Omega} + \frac{Gr}{Re^2}\nabla\times\Theta\hat{\mathbf{g}} = 0 \tag{9}$$

$$\frac{\partial\Theta}{\partial t} + (\mathbf{u}\cdot\nabla)\Theta - \frac{1}{RePr}\nabla^2\Theta = 0 \tag{10}$$

The formulation is subjected to the initial and boundary conditions,

$$\boldsymbol{\Omega}(\mathbf{x},0) = \nabla\times\mathbf{u}(\mathbf{x},0) \tag{11}$$

$$\mathbf{u}(\mathbf{x}_S,t) = \mathbf{b}(\mathbf{x}_S,t) \tag{12}$$

$$\Theta(\mathbf{x}_{\tilde{S}},t) = \mathbf{f}(\mathbf{x}_{\tilde{S}},t) \tag{13}$$

$$(\hat{\mathbf{n}}\cdot\nabla)\mathbf{u}_C = 0 \tag{14}$$

$$\hat{\mathbf{n}}\cdot\nabla\Theta|_{\tilde{C}} = 0 \tag{15}$$

$$(\hat{\mathbf{n}}\cdot\nabla)\boldsymbol{\Omega}|_C = 0 \tag{16}$$

$$\nabla\cdot\mathbf{u}(\mathbf{x}_S,t) = 0 \tag{17}$$

$$\nabla\cdot\boldsymbol{\Omega}(\mathbf{x}_S,t) = 0 \tag{18}$$

$$\mathbf{n}\cdot\boldsymbol{\Omega}(\mathbf{x}_S,t) = \mathbf{n}\cdot\nabla_S\times\mathbf{b}(\mathbf{x}_S,t) \tag{19}$$

where $\hat{\mathbf{n}}$ is the unit normal to the boundary, $\tilde{S}$ is the boundary surface segment with a known temperature, $\mathbf{f}$, $\tilde{C}$ is the heat flux boundary which is assumed to be adiabatic for simplicity, S is the boundary surface segment for a known velocity field, $\mathbf{x}_S$ is a spatial point on S, $\mathbf{b}$ is the boundary velocity, and C is the outflow boundary. When the boundary is a rigid no-slip solid wall in contact with the fluid, the boundary velocity, $\mathbf{b}$, is zero.

The initial-boundary value formulation (Equations (8)–(19)) thus consists of three Poisson equations coupling the velocity and vorticity components kinematically, with the continuity constraint, three vorticity transport equations describing flow kinetics, and an energy transport equation. Gunzburger and Peterson [12] point out that the problem is well-posed. However,

to solve the velocity–vorticity equation system successfully, the boundary condition (19) must be implemented, the kinematic component of the equation $\mathbf{\Omega} = \nabla \times \mathbf{u}$ normal to S. Then, the equivalence of the velocity–vorticity formulation with the original primitive variable form is assured [13].

2.2. Boundary conditions

Boundary conditions for the velocity Poisson equations are readily available. At the inflow boundary, a Dirichlet boundary condition is imposed for a known inlet velocity profile. A homogeneous Neumann boundary condition may be applied at the flow exit. On solid walls, no-slip boundary conditions with $\mathbf{b} = \mathbf{0}$ in Equation (12) are appropriate.

In an open square channel, the velocity and vorticity profiles at the inlet are prescribed with the assumption that $(\partial w/\partial x) = 0 = (\partial w/\partial y)$. A homogeneous Neumann boundary condition for vorticity may be enforced at a flow exit. However, careful determination of the vorticity discrete form of the kinematic boundary condition (Equation (19)) at a no-slip wall is critical.

Guj and Stella [14] indicate that a solenoidal velocity field for an arbitrary vorticity distribution may be assured only by coupling the solution process for the velocity Poisson and the vorticity transport equations. Daube [6] also points out that the requirement to satisfy the continuity equation reduces to the boundary condition coupling the velocity and vorticity at a wall. Therefore, conservation of mass, hence the conservation of the solenoidality of vorticity field, must be enforced implicitly in the bulk of the flow by the kinematic velocity Poisson equations, and also imposed explicitly on the boundary of the fluid domain by the kinematic vorticity boundary condition.

A second order accurate finite difference vorticity kinematic boundary condition is developed [15] to complete this formulation. From Equation (19), the vorticity at a no-slip wall is represented by

$$\mathbf{\Omega}_{\text{wall}} = \hat{\mathbf{n}} \cdot \nabla_S \times \mathbf{u} \tag{20}$$

A schematic diagram of a typical flow geometry is shown in Figure 1, where $w0, w1$, and $w2$ represent the computational node points on the wall, next to the wall, and second next to the wall, respectively, along an axis locally normal to the boundary plane.

For the wall normal parallel to the x-axis, from Equations (20) and (4), the vorticity components at the wall are

$$\Omega_x = 0, \quad \Omega_y = -\frac{\partial w}{\partial x}, \quad \Omega_z = \frac{\partial v}{\partial x} \tag{21}$$

For the wall normal to the y-axis, the vorticity components are

$$\Omega_x = \frac{\partial w}{\partial y}, \quad \Omega_y = 0, \quad \Omega_z = -\frac{\partial u}{\partial y} \tag{22}$$

hence for the z-axis,

$$\Omega_x = -\frac{\partial v}{\partial z}, \quad \Omega_y = \frac{\partial u}{\partial z}, \quad \Omega_z = 0 \tag{23}$$

The kinematic vorticity boundary condition is imposed following the finite element assembly process by replacement of the discretized nodal vorticity equation weak statement from Equation (9) at the wall node. These vorticity kinematic equations are obtained via a Taylor series

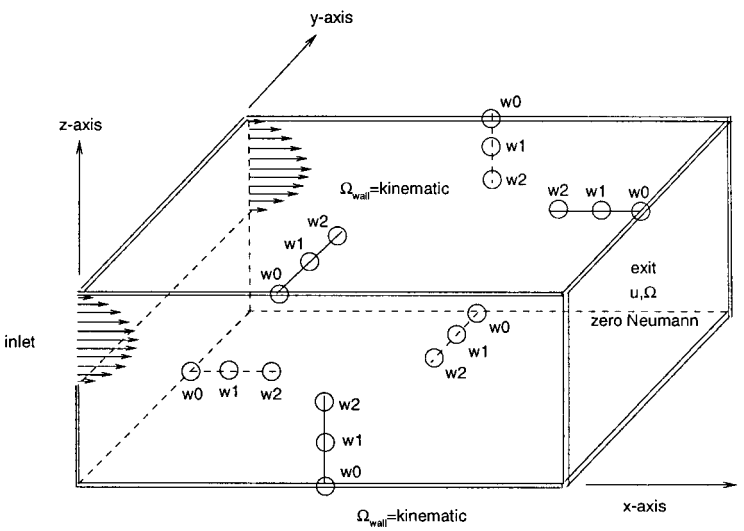

Figure 1. Schematic diagram of kinematic vorticity boundaries.

expansion of equations (Equation (20)). A detailed description of derivation for one of the equations follows; the remainder are given in Reference [15].

The Taylor series expansion for the x-velocity component, u, for the wall normal parallel to the z-axis is

$$u_{w1} = u_{w0} + \Delta z \frac{\mathrm{d}u_{w0}}{\mathrm{d}z} + \frac{\Delta z^2}{2} \frac{\mathrm{d}^2 u_{w0}}{\mathrm{d}z^2} + \mathcal{O}(\Delta z)^3 \tag{24}$$

Using Equation (23)

$$u_{w1} = u_{w0} + \Delta z \Omega_{y,w0} + \frac{\Delta z^2}{2} \frac{\mathrm{d}\Omega_{y,w0}}{\mathrm{d}z} + \mathcal{O}(\Delta z)^3 \tag{25}$$

Expanding $\Omega_{y,w1}$ in terms of $\Omega_{y,w0}$

$$\Omega_{y,w1} = \Omega_{y,w0} + \Delta z \frac{\mathrm{d}\Omega_{y,w0}}{\mathrm{d}z} + \mathcal{O}(\Delta z)^2 \tag{26}$$

Combining Equations (25) and (26),

$$u_{w1} = u_{w0} + \Delta z \Omega_y + \frac{\Delta z^2}{2} \left(\frac{\Omega_{y,w1} - \Omega_{y,w0}}{\Delta z} \right) + \mathcal{O}(\Delta z)^3 \tag{27}$$

the result is

$$(\Omega_{y,w1} + \Omega_{y,w0}) - \frac{2}{\Delta z}(u_{w1} - u_{w0}) + \mathcal{O}(\Delta z)^2 = 0 \tag{28}$$

Hence, for the wall normal parallel to the positive x-axis, the resultant vorticity kinematic equations are,

$$\Omega_{x,w0} = 0 \tag{29}$$

$$(\Omega_{y,w1} + \Omega_{y,w0}) + \frac{2}{\Delta x}(w_{w1} - w_{w0}) = 0 \tag{30}$$

$$(\Omega_{z,w1} + \Omega_{z,w0}) - \frac{2}{\Delta x}(v_{w1} - v_{w0}) = 0 \tag{31}$$

For the wall normal parallel to the negative x-axis, the vorticity kinematic equations are,

$$\Omega_{x,w0} = 0 \tag{32}$$

$$(\Omega_{y,w1} + \Omega_{y,w0}) - \frac{2}{\Delta x}(w_{w1} - w_{w0}) = 0 \tag{33}$$

$$(\Omega_{z,w1} + \Omega_{z,w0}) + \frac{2}{\Delta x}(v_{w1} - v_{w0}) = 0 \tag{34}$$

3. WEAK STATEMENT ALGORITHM

3.1. Galerkin weak statement

With the semi-discrete finite element approximation of the state variable,

$$\mathbf{q}(\mathbf{x}, t) \approx \mathbf{q}^h \equiv \sum_{j=1}^{m} N_j(\mathbf{x})^t \mathbf{Q}_j(t) \tag{35}$$

$$\mathbf{q} = \{\mathbf{u}, \boldsymbol{\Omega}, \boldsymbol{\Theta}\}, \quad \mathbf{Q} = \{\mathbf{U}, \mathbf{O}, T\}, \quad \mathbf{U} = \{U, V, W\}, \quad \mathbf{Q} = \{O_x, O_y, O_z\} \tag{36}$$

the Galerkin weak statement is obtained by minimizing the residual error over the discretized domain, σ^h, with the weight function identical to the trial function, $N_j(\mathbf{x})$, is

$$GWS(\mathbf{u}^h) \equiv \{F\mathbf{U}\} = \int_{\sigma^h} \{N\}(\nabla^2 \mathbf{u}^h + \nabla \times \boldsymbol{\Omega}^h) \mathrm{d}V = 0 \tag{37}$$

$$GWS(\boldsymbol{\Omega}^h) \equiv \{F\mathbf{O}\} = \int_{\sigma^h} \{N\} \left(\frac{\partial \boldsymbol{\Omega}^h}{\partial t} + (\mathbf{u}^h \cdot \nabla)\boldsymbol{\Omega}^h - (\boldsymbol{\Omega}^h \cdot \nabla)\mathbf{u}^h - \frac{1}{Re} \nabla^2 \boldsymbol{\Omega}^h + \frac{Gr}{Re^2} \nabla \times \Theta^h \hat{\mathbf{g}} \right) \mathrm{d}V = 0 \tag{38}$$

$$GWS(\Theta^h) \equiv \{FT\} = \int_{\sigma^h} \{N\} \left(\frac{\partial \Theta^h}{\partial t} + (\mathbf{u}^h \cdot \nabla)\boldsymbol{\Theta}^h - \frac{1}{RePr} \nabla^2 \Theta^h \right) \mathrm{d}V = 0 \tag{39}$$

Substituting Equation (35) for $\mathbf{u}^h$ and $\boldsymbol{\Omega}^h$ and dropping all surface integrals for Dirichlet and homogeneous Neumann boundary conditions after applying the Green Gauss theorem,

Equations (37)–(39) become of the form

$$\{FU\} = \mathscr{S}_{e=1}^{M}\{[c2kke]\{U\}_e + [c20ze]\{O_y\}_e - [c20ye]\{O_z\}_e\} = 0 \tag{40}$$

$$\{FV\} = \mathscr{S}_{e=1}^{M}\{[c2kke]\{V\}_e + [c20xe]\{O_z\}_e - [c20ze]\{O_x\}_e\} = 0 \tag{41}$$

$$\{FW\} = \mathscr{S}_{e=1}^{M}\{[c2kke]\{W\}_e + [c20ye]\{O_x\}_e - [c20xe]\{O_y\}_e\} = 0 \tag{42}$$

$$\begin{aligned}\{FO_x\} = \mathscr{S}_{e=1}^{M}\Bigg\{&[c200e]\frac{\mathrm{d}\{O_x\}_e}{\mathrm{d}t} + (\{U\}_e^T[c30x0e] + \{V\}_e^T[c30y0e] \\ &+\{W\}_e^T[c30z0e])\{O_x\}_e - (\{O_x\}_e^T[c30x0e] + \{O_y\}_e^T[c30y0e] \\ &+\{O_z\}_e^T[c30z0e])\{U\}_e + \frac{1}{Re}[c2kke]\{O_x\}_e - \frac{Gr}{Re^2}[c20ye]\{T\}_e\Bigg\} = 0\end{aligned} \tag{43}$$

$$\begin{aligned}\{FO_y\} = \mathscr{S}_{e=1}^{M}\Bigg\{&[c200e]\frac{\mathrm{d}\{O_y\}_e}{\mathrm{d}t} + (\{U\}_e^T[c30x0e] + \{V\}_e^T[c30y0e] \\ &+\{W\}_e^T[c30z0e])\{O_y\}_e - (\{O_x\}_e^T[c30x0e] + \{O_y\}_e^T[c30y0e] \\ &+\{O_z\}_e^T[c30z0e])\{V\}_e + \frac{1}{Re}[c2kke]\{O_y\}_e + \frac{Gr}{Re^2}[c20xe]\{T\}_e\Bigg\} = 0\end{aligned} \tag{44}$$

$$\begin{aligned}\{FO_z\} = \mathscr{S}_{e=1}^{M}\Bigg\{&[c200e]\frac{\mathrm{d}\{O_z\}_e}{\mathrm{d}t} + (\{U\}_e^T[c30x0e] + \{V\}_e^T[c30y0e] \\ &+\{W\}_e^T[c30z0e])\{O_z\}_e - (\{O_x\}_e^T[c30x0e] + \{O_y\}_e^T[c30y0e] \\ &+\{O_z\}_e^T[c30z0e])\{W\}_e + \frac{1}{Re}[c2kke]\{O_z\}_e\Bigg\} = 0\end{aligned} \tag{45}$$

$$\begin{aligned}\{FT\}_e = \mathscr{S}_{e=1}^{M}\Bigg\{&[c200e]\frac{\mathrm{d}\{T\}_e}{\mathrm{d}t} + (\{U\}_e^T[c30x0e] + \{V\}_e^T[c30y0e] \\ &+\{W\}_e^T[c30z0e])\{T\}_e + \frac{1}{RePr}[c2kke]\{T\}_e\Bigg\} = 0\end{aligned} \tag{46}$$

For any choice of trial space basis $\{N\}$, the defined element-rank matrices are

$$[c2kke] = \int_{\sigma_e} \nabla\{N\} \cdot \nabla\{N\}^T \,\mathrm{d}V \tag{47}$$

$$[c20xe] = \int_{\sigma_e} \{N\}\frac{\partial\{N\}^T}{\partial x}\,\mathrm{d}V \tag{48}$$

$$[c20ye] = \int_{\sigma_e} \{N\}\frac{\partial\{N\}^T}{\partial y}\,\mathrm{d}V \tag{49}$$

$$[c20ze] = \int_{\sigma_e} \{N\}\frac{\partial\{N\}^T}{\partial z}\,\mathrm{d}V \tag{50}$$

$$[c200e] = \int_{\sigma_e} \{N\}\{N\}^T \, \mathrm{d}V \tag{51}$$

$$[c30x0e] = \int_{\sigma_e} \{N\} \frac{\partial \{N\}}{\partial x} \{N\}^T \, \mathrm{d}V \tag{52}$$

$$[c30y0e] = \int_{\sigma_e} \{N\} \frac{\partial \{N\}}{\partial y} \{N\}^T \, \mathrm{d}V \tag{53}$$

$$[c30z0e] = \int_{\sigma_e} \{N\} \frac{\partial \{N\}}{\partial z} \{N\}^T \, \mathrm{d}V \tag{54}$$

3.2. Newton statement

The semi-discretized finite element velocity–vorticity weak statements form the following system of algebraic-ordinary differential equations,

$$\{F\mathbf{U}\} = \{R\mathbf{U}\} = 0 \tag{55}$$

$$\{F\mathbf{O}\} = [M]\frac{\mathrm{d}\{\mathbf{O}\}}{\mathrm{d}t} + \{R\mathbf{O}\} = 0 \tag{56}$$

$$\{FT\} = [M]\frac{\mathrm{d}T}{\mathrm{d}t} + \{RT\} = 0 \tag{57}$$

where $[M]$ is the global (assembled) mass matrix associated with the time term and $\{R\mathbf{Q}\}$ is the global steady state residual representing all other weak statement terms. Equations (56) and (57) are systems of ordinary differential equations, for which the θ-implicit, one step Euler scheme is used to integrate through the transient solution. The terminal computable algebraic statements are then,

$$\{F\mathbf{U}\} = \{R\mathbf{U}\} = [D]\{\mathbf{U}\} + \{S(\mathbf{O})\} = 0 \tag{58}$$

$$\{F\mathbf{O}\} = [M]\{\mathbf{O}_{n+1} - \mathbf{O}_n\} + \Delta t\{R\mathbf{O}\}_{n+\theta} = 0 \tag{59}$$

$$\{FT\} = [M]\{T_{n+1} - T_n\} + \Delta t\{RT\}_{n+\theta} = 0 \tag{60}$$

where n denotes the times station t_n, $t_{n+1} = t_n + \Delta t$, and $\theta = 0.5$ represents the trapezoidal rule while $\theta = 1$ represents the fully implicit backward Euler integration scheme.

The residual vector $\{R\mathbf{Q}\}$ is a nonlinear function of the nodal state variable members $\mathbf{U}, \mathbf{O}$ and T. Thus, Equations (58)–(60), along with Equation (19), represent a coupled, nonlinear system of algebraic equations that must be solved iteratively. The Newton–Raphson algorithm is used and the subsequent procedure is

$$\{\mathbf{Q}\}^0_{n+1} = \{\mathbf{Q}\}_n; \quad \mathbf{Q} \equiv (U, V, W, O_x, O_y, O_z, T)$$

$$\{F\mathbf{Q}\}^0_{n+1} = \{F\mathbf{Q}\}_n \quad \text{for } p = 0, 1, 2, \ldots \text{ until convergence at time } n+1$$

$$[JAC] = [J\mathbf{QQ}] = \left[\frac{\partial\{F\mathbf{Q}\}}{\partial\{\mathbf{Q}\}}\right]^{p}_{n+1}$$

$$[JAC]\{\delta\mathbf{Q}\}^{p+1}_{n+1} = -\{F\mathbf{Q}\}^{p}_{n+1}$$

$$\{\mathbf{Q}\}^{p+1}_{n+1} = \{\mathbf{Q}\}^{p}_{n+1} + \{\delta\mathbf{Q}\}^{p+1}_{n+1}$$

where [JAC], the jacobian matrix of the terminal non-linear algebraic statement, is symbollically

$$[JAC] = [JQQ] = \begin{bmatrix} JUU & 0 & 0 & 0 & JUO_y & JUO_z & 0 \\ 0 & JVV & 0 & JVO_x & 0 & JVO_z & 0 \\ 0 & 0 & JWW & JWO_x & JWO_y & 0 & 0 \\ JO_xU & JO_xV & JO_xW & JO_xO_x & JO_xO_y & JO_xO_z & JO_xT \\ JO_yU & JO_yV & JO_yW & JO_yO_x & JO_yO_y & JO_yO_z & JO_yT \\ JO_zU & JO_zV & JO_zW & JO_zO_x & JO_zO_y & JO_zO_z & 0 \\ JTU & JTV & JTW & 0 & 0 & 0 & JTT \end{bmatrix}$$

3.3. *Vorticity kinematic boundary conditions*

The general form of the vorticity kinematic equations are,

$$\begin{aligned} f(O_{\text{wall}}) = {} & a_{x0}O_{x,w0} + a_{x1}O_{x,w1} + a_{y0}O_{y,w0} + a_{y1}O_{y,w1} \\ & + a_{z0}O_{z,w0} + a_{z1}O_{z,w1} + b_{x0}u_{w0} + b_{x1}u_{w0} \\ & + b_{y0}v_{w0} + b_{y1}v_{w1} + b_{z0}w_{w0} + b_{z1}w_{w1} = 0 \end{aligned} \tag{61}$$

For example, for Equation (28) the coefficients are

$$a_{x0} = a_{x1} = a_{z0} = a_{z1} = b_{y0} = b_{y1} = b_{z0} = b_{z1} = 0$$

$$a_{y0} = a_{y1} = 1, \quad b_{x0} = \frac{2}{\Delta z}, \quad b_{x1} = -\frac{2}{\Delta z}$$

To apply the kinematic vorticity boundary conditions, the weak statement residual vorticity equations at the boundary nodes where no-slip velocity is imposed are replaced by the Equation (52). The entire row of the corresponding vorticity component at the boundary node is zeroed out in the jacobian matrix and replaced appropriately by the coefficients a and b of

$f(\Omega_{\text{wall}})$ at the corresponding entries.

$(\mathbf{q})$	(u)	(v)	(w)	(Ω_x)	(Ω_y)	(Ω_z)
$(\cdots)$	$\cdots$	$\cdots$	$\cdots$	$\cdots$	$\cdots$	$\cdots$
(Ω_y)	JO_yU	JO_yV	JO_yW	JO_yO_x	JO_yO_y	JO_yO_z
$(\Omega_{y,\text{wall}})$	$0\cdots, b_{x0}, b_{x1}, \cdots 0$	$\cdots 0 \cdots$	$\cdots 0 \cdots$	$\cdots 0 \cdots$	$0\cdots, a_{y0}, a_{y1}, \cdots 0$	$\cdots 0 \cdots$
(Ω_y)	JO_yU	JO_yV	JO_yW	JO_yO_x	JO_yO_y	JO_yO_z
$(\cdots)$	$\cdots$	$\cdots$	$\cdots$	$\cdots$	$\cdots$	$\cdots$

4. COMPUTATIONAL PROCEDURE

Parallel computation is carried out on the IBM SP2 at the University of Tennessee (UT), which has 24 thin nodes and two high nodes. Only the thin nodes are utilized for parallel computations. Each thin node has 256 MB of memory and is based on a 120 MHz POWER2 SC chip capable of delivering 480 million floating point operations per second (MFLOPS). A Single Program Multiple Data (SPMD) computer code was written in FORTRAN in conjunction with Message Passing Interface (MPI) communications library.

The terminal Newton jacobian for the fully coupled velocity–vorticity formulation is a 7×7 block matrix. Each jacobian block is a sparse matrix with a large number of zeros. A compressed row storage scheme is used to minimize memory storage.

The BiCGSTAB sparse Krylov solver is used to compute the solution of $Ax = b$ where $A \equiv [JQQ]$, $x \equiv \delta Q$, and $b \equiv -FQ$. The major kernel of the solver is a matrix vector multiplication operation which can be efficiently implemented on the IBM SP2. The stopping criterion [16] for these iteration methods is

$$\|r_k\|_\infty < \varepsilon \|b\|_\infty \tag{62}$$

where ε is the error tolerence relative to $\|b\|$, the magnitude of the right hand side residual vector. For the three dimensional flow simulations reported herein, conducted in this project, ε is chosen to be 10^{-10}. In this implementation, the Jacobi (diagonal scaling) preconditioner, $Q = [\text{diag}(A)]^{-1}$, is used. The effect of this preconditioning may be small, however it can be efficiently implemented in parallel.

5. RESULTS AND DISCUSSIONS

5.1. Square channel flow

Three test cases are selected to verify and benchmark performance of the developed parallel velocity–vorticity finite element formulation for the 3D incompressible Navier–Stokes equations. Fully developed, and developing flow in a straight rectangular channel tests validity and accuracy of the algorithm boundary conditions and the constraint of continuity. The

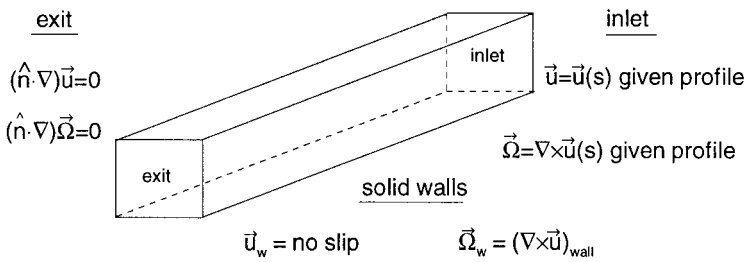

Figure 2. Boundary condition for straight channel flow.

verification steady state fully developed axial (u)-velocity distribution is [17]

$$u = \frac{48}{\pi^3}\frac{\xi_u(y,z,h)}{\varphi} \tag{63}$$

$$\xi_u(y,z,h) = \sum_{n=1,3,5}^{N} (-1)^{\frac{n-1}{2}} \left[1 - \frac{\cosh(n\pi y/2h)}{\cosh(n\pi/2)}\right] \frac{\cos(n\pi z/2h)}{n^3} \tag{64}$$

$$\varphi = 1 - \frac{192}{\pi^5} \sum_{n=1,3,5}^{N} \frac{\tanh(n\pi/2)}{n^5} \tag{65}$$

where h is the duct half-height and N is a large integer, e.g., $N = 200$ is used. The uniform trilinear basis discretization consists of $M = 16 \times 16 \times 16$ elements yielding 4913 nodes and 4096 hexahedral elements. For boundary conditions (Figure 2) the steady state analytical velocity and vorticity profiles are prescribed across the inlet, and vanishing Neumann conditions for velocity and vorticity are exact and imposed at the exit plane. Boundary conditions for the velocity at channel walls are no-slip, hence the kinematic vorticity boundary condition (Equations (21)–(34)) generalized for wall normal variation, is imposed. The state variable inside the channel is initialized at zero. A large time step size is taken using the backward Euler integration rule to compute the steady state solution in a single time step.

The computed center plane solution for the 3D square duct is shown in Figure 3. The entrance velocity profile is propagated throughout the channel to four significant digits. These data clearly verify that the chosen velocity–vorticity formulation, with the derived second order vorticity kinematic boundary condition, is indeed mass conserving. Solutions of the developing channel flow with a slug inlet profile is shown in Figure 4.

5.2. *Lid-driven cavity*

The lid-driven cavity is a classic 2D benchmark for laminar incompressible flow. With the increase of computing capability in recent years, the lid-driven cavity problem has matured as a standard *Re*-dependent benchmark for 3D incompressible Navier–Stokes algorithms, c.f. References [10, 14, 18–21].

The 3D cavity is a unit cube, with the top wall moving parallel to the positive x-axis at unit velocity, $u = 1$. The vorticity boundary conditions are kinematic on every node on the cube walls. The initial condition is zero vorticity everywhere. The top plate velocity generates

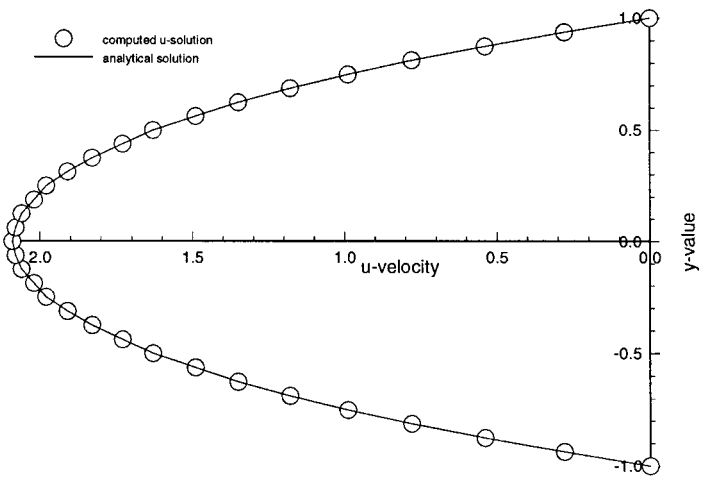

Figure 3. Initial condition and predicted steady state center plane 3D fully developed channel flow.

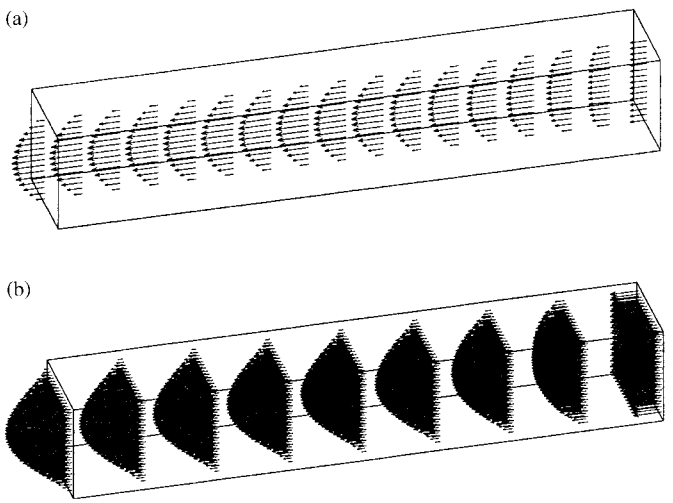

Figure 4. Velocity profile at the center plane, and planar perspectives, for 3D square channel flow, $Re = 100$.

vorticity which propagates throughout until the flow field reaches a steady state. In the present study, steady state solutions for $Re = 100$, $Re = 400$, and $Re = 1000$ are computed.

Significant computational resources are required to resolve the complexity of the 3D driven cavity benchmark. A solution-adapted nonuniform cartesian $M = 48 \times 48 \times 48$ mesh was selected, following coarser mesh tests [15], which contains 110 592 trilinear elements, and the isothermal Newton statement contains 705 894 equations. The discretized domain is decomposed into 12 equal blocks on the y-axis. Each block of $M = 48 \times 4 \times 48$ mesh is assigned to a processor on the IBM SP2. The total memory requirement is approximately 930 Mbytes, and 78 Mbytes of local processor memory is required.

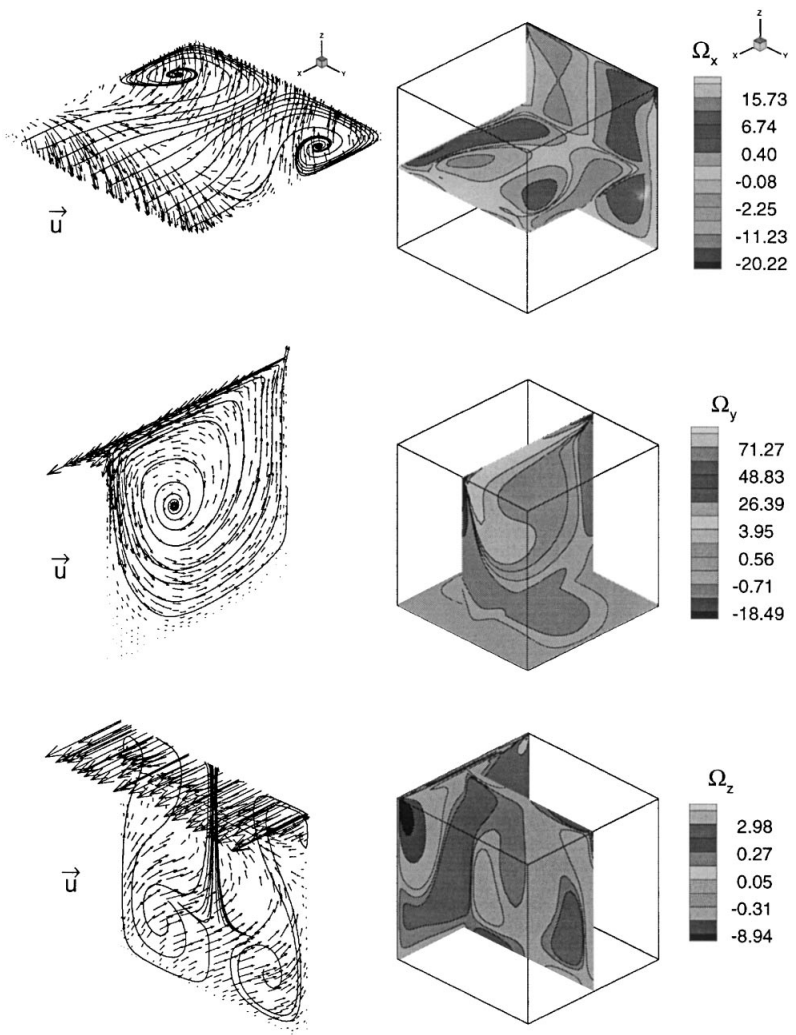

Figure 5. Perspective 3D solution summary for driven cavity problem, $Re = 400$.

The 3D sectional perspective views for the computed velocity vector and vorticity fields for $Re = 400$ is shown in Figure 5. The vorticity plots at x-mid-plane for Ω_x, y-mid-plane for Ω_y, and z-mid-plane for Ω_z fully illustrate the transport of flow information. Contour lines of the appropriate vortices shown on each mid-plane on the velocity vector plots correspond to the 2D streamtraces projected from the 3D velocity vector field.

Two dimensional planar projections of the velocity vector field at $Re = 100$, $Re = 400$, and $Re = 1000$ on the three centroidal planes of the cube are shown in Figure 6. The axis of the primary vortex starts in the upper right half region, then gradually moves towards the cube center as the Reynolds number increases. The flow is fully three

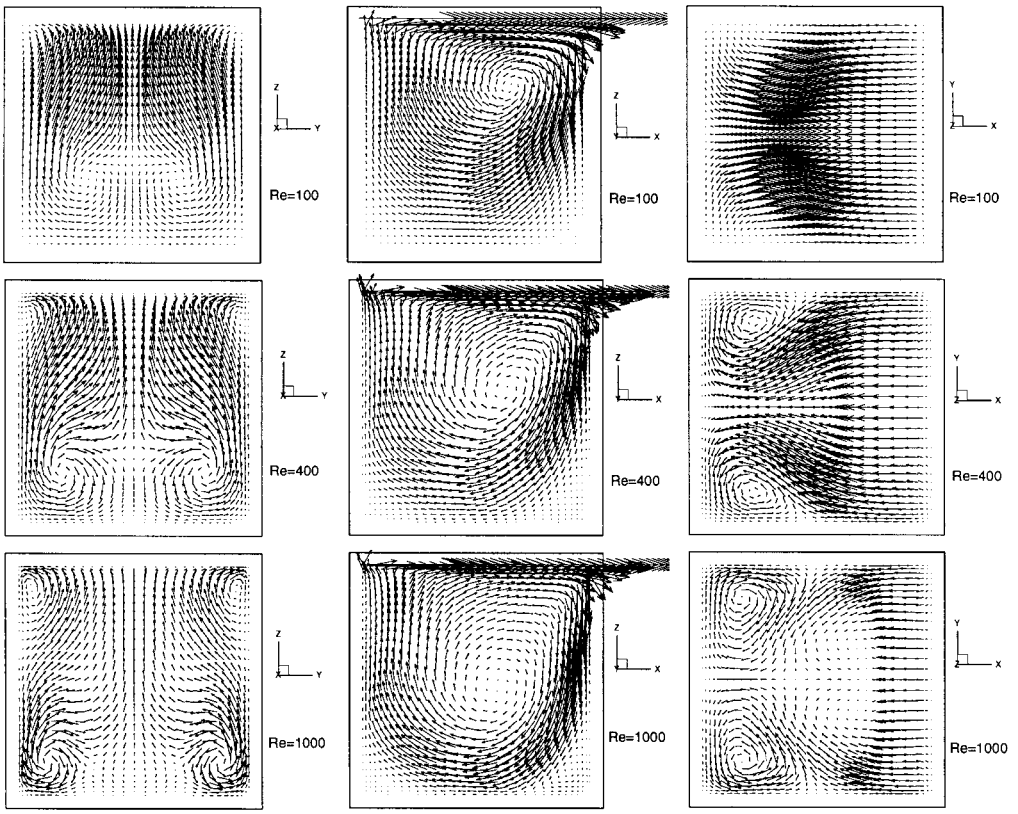

Figure 6. 2D planar projections of mid-plane velocity vector field for 3D driven cavity, $Re = 100, 400, 1000$.

dimensional such that secondary vortices turn sidewards in the y-direction and upwards in the z-direction.

As can be seen in the velocity vector plot on the $y-z$ centroidal plane, a pair of vortices appear near the centerline and move out towards the lower corners as the Reynolds number increases. Two small recirculation cells are also emerging at the top corners as the Reynolds number goes through $Re = 400$ to $Re = 1000$.

As for the $x-y$ centroidal plane, at $Re = 100$ the flow is returning normally along the $x-y$ boundary. However, at $Re = 400$, the flow is now turning in the z-direction, which results in a pair of 2D projected vortices from the 3D velocity vectors. A second pair of projected vortices also appears as the Reynolds number reaches 1000 (Figure 6). Similar velocity vector patterns for $Re = 100$, $Re = 400$, and $Re = 1000$, are reported by Guj and Stella [14], Fujima *et al.* [19], and Jiang *et al.* [21].

The u-velocity component distribution on the vertical plane centerline has been used as a measure of solution accuracy for the 3D lid-driven cavity benchmark. For $Re = 100$, this u-velocity component data reported by Ku *et al.* [18], Guj and Stella [10], Fujima *et al.* [19], and

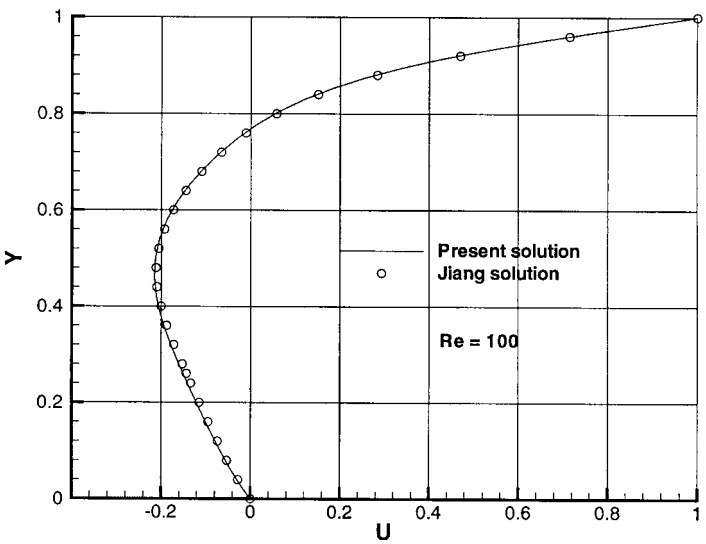

Figure 7. 3D mid-plane centerline u-velocity comparison, $Re = 100$.

Jiang *et al.* [21] agree quite well with each other. The computed solution from the present formulation is shown in Figure 7. The present solution matches almost exactly with Jiang *et al.* [21]. Very close agreement of the u-velocity value is seen across the entire span of the vertical z-axis, see Table I. The maximum difference is 1.4 per cent at the peak value.

5.3. *Parallel implementation performance*

For this present algorithm, the flow field at $Re = 100$ is started from rest, and the code could produce the steady-state solution using a single large time step, $\Delta t = 100$. A timing test for the testcase is conducted on the IBM SP2 with 12 processing nodes. It takes an average of 0.7 s elapsed wall-clock time to complete one single BiCGSTAB iteration with Jacobi preconditioner. An average of 18 s elapsed time is needed to form and assemble the jacobian matrix and residual vectors for each Newton step. Another 160 s is estimated for the overheads. For $Re = 100$, 11 Newton steps and a total of 2995 BiCGSTAB iterations are required to converge the extremum Newton error, $\delta Q_{\max}$ to 7.5×10^{-6} for Ω_y. Consequently, a total of 41 min on the SP2 was needed to achieve the reported steady-state solution.

For $Re = 400$, the admissible time step, $\Delta t = 2.0$, was substantially smaller. After 25 time steps, the steady state is accepted with an extremum Newton residual of $\delta Q = 4.77 \times 10^{-5}$ for the Ω_y component. The number of Newton iterations was 113 with 31 065 BiCGSTAB iterations. The centerline u-velocity profile of the present algorithm on the non-uniform $M = 48 \times 48 \times 48$ mesh solution is compared with Jiang *et al.* [21] and Fujima *et al.* [19] in Figure 8. The negative peak u-velocity predicted by Jiang is 0.2341 while 0.2349 is predicted by the present algorithm. The agreement is within 0.4 per cent.

For $Re = 1000$, the admissible time step is further reduced to $\Delta t = 0.1$. After 52 time steps, the steady state was accepted with an extremum $\delta Q = 1.45 \times 10^{-4}$, requiring 237 Newton

Table I. U-velocity along the vertical centerline of the 3D driven cavity.

z location	$Re = 100$	$Re = 400$	$Re = 1000$
1.00	1.0	1.0	1.0
0.9991	0.9937	0.9893	0.9836
0.9965	0.9747	0.9570	0.9345
0.9922	0.9430	0.9032	0.8535
0.9861	0.8986	0.8286	0.7443
0.9783	0.8417	0.7358	0.6164
0.9688	0.7732	0.6304	0.4851
0.9575	0.6947	0.5207	0.3676
0.9444	0.6087	0.4162	0.2763
0.9297	0.5184	0.3256	0.2144
0.9132	0.4276	0.2540	0.1764
0.8950	0.3399	0.2019	0.1530
0.8750	0.2583	0.1663	0.1369
0.8533	0.1848	0.1419	0.1237
0.8299	0.1200	0.1242	0.1116
0.8047	0.0633	0.1097	0.1001
0.7778	0.0137	0.0965	0.0891
0.7491	−0.0301	0.0836	0.0786
0.7188	−0.0695	0.0704	0.0684
0.6866	−0.1051	0.0564	0.0586
0.6528	−0.1370	0.0411	0.0488
0.6172	−0.1648	0.0238	0.0392
0.5799	−0.1874	0.0036	0.0294
0.5408	−0.2040	−0.0206	0.0192
0.5	−0.2135	−0.05	0.0083
0.4592	−0.2154	−0.0836	−0.0038
0.4201	−0.2109	−0.1190	−0.0174
0.3828	−0.2018	−0.1540	−0.0337
0.3472	−0.1897	−0.1856	−0.0539
0.3134	−0.1759	−0.2108	−0.0792
0.2812	−0.1614	−0.2275	−0.1101
0.2509	−0.1469	−0.2349	−0.1462
0.2222	−0.1327	−0.2336	−0.1849
0.1953	−0.1191	−0.2250	−0.2218
0.1701	−0.1061	−0.2111	−0.2522
0.1467	−0.0938	−0.1937	−0.2719
0.1250	−0.0820	−0.1744	−0.2792
0.1050	−0.0708	−0.1541	−0.2749
0.0868	−0.0620	−0.1337	−0.2608
0.0703	−0.0501	−0.1134	−0.2390
0.0556	−0.0407	−0.0935	−0.2106
0.0425	−0.0320	−0.0745	−0.1772
0.0312	−0.0241	−0.0568	−0.1407
0.0217	−0.0171	−0.0407	−0.1039
0.0139	−0.0111	−0.0268	−0.0697
0.0078	−0.0064	−0.0154	−0.0406
0.0035	−0.0029	−0.0690	−0.185
0.0009	−0.0007	−0.0018	−0.047
0.0000	0.0	0.0	0.0

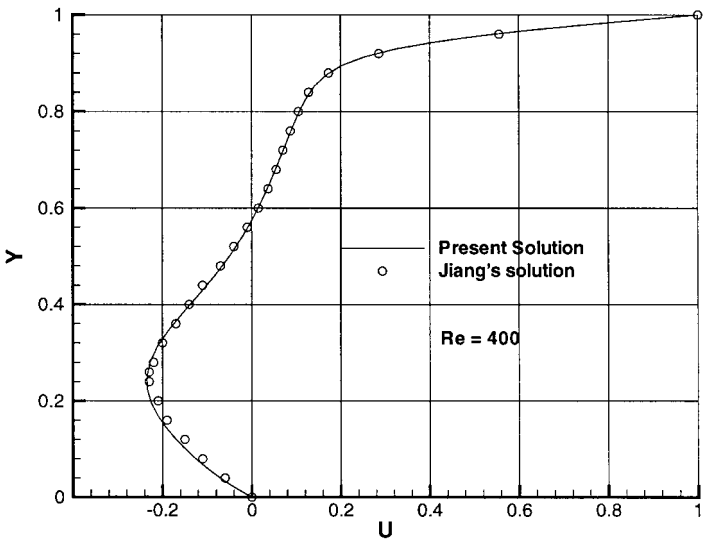

Figure 8. 3D mid-plane centerline u-velocity comparison, $Re = 400$.

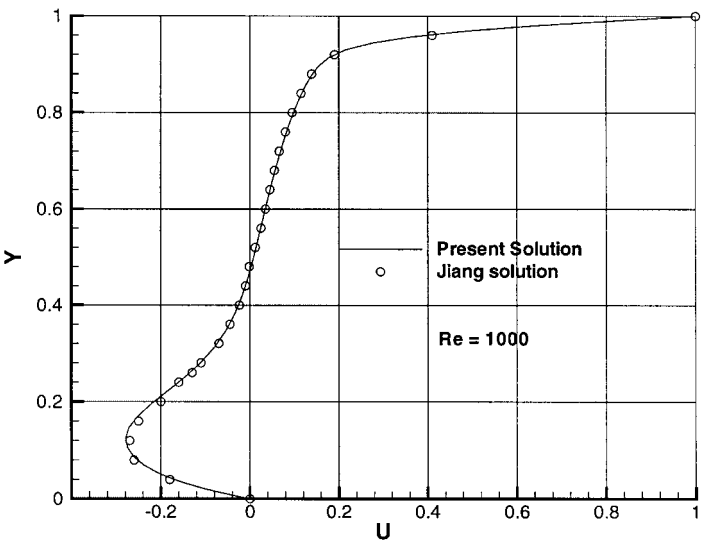

Figure 9. 3D mid-plane centerline u-velocity comparison, $Re = 1000$.

steps. The symmetric centerplane solution is compared with Jiang *et al.* [21] in Figure 9. The negative peak u-velocity predicted by Jiang is -0.275. The present algorithm value for minimum u is -0.279, and both solutions are in very close agreement across the entire vertical span.

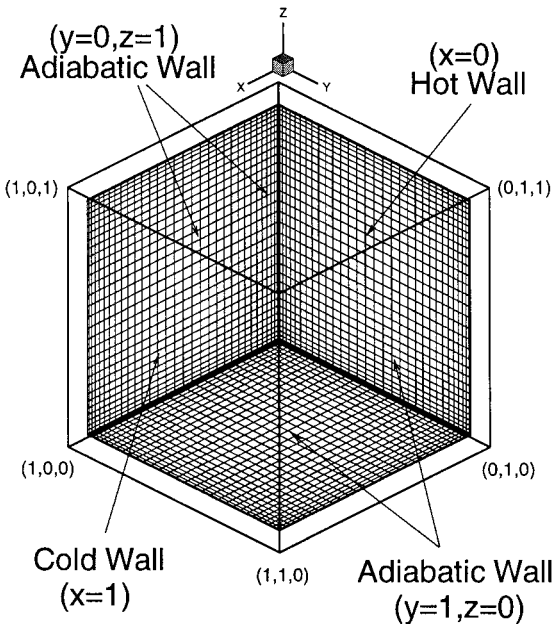

Figure 10. Non-uniform finite element mesh for 3D thermal cavity.

5.4. *Thermal-driven cavity*

Buoyancy driven flow due to natural convention is an enclosed 3D rectangular box is the direct extension of the 2D thermal cavity benchmark. Solutions are parameterized by the Rayleigh number, $Ra = PrGr$, for the potential temperature boundary conditions of one and zero on the front and back walls, along the x-axis, while both side walls along the y-axis and the floor and ceiling are adiabatic (Figure 10). Velocity boundary conditions are all no-slip, and the kinematic vorticity boundary condition is imposed at every boundary node.

The first numerical solution of the 3D thermal cavity problem is reported by Millinson and de Vahl Davis [22]. Using the Continuity Constraint Method, Williams [23] presents a solution for the so-called 'window cavity problem' at $Ra = 1.5 \times 10^5$. A numerical study of 3D natural convection for air in the cubic enclosure is reported in Reference [24] for Rayleigh number from 10^3 to 10^6 using a control-volume-based finite difference staggered mesh procedure together with a pressure correction algorithm.

The three Poisson equations, three momentum equations with Boussinesq term, and the energy equation are solved simultaneously. The solution-adapted non-uniform cartesian $M = 48 \times 48 \times 48$ mesh is decomposed into eight rectangular subregions which are assigned to eight processors for computation on the IBM SP2. The total number of equations is 823,543. Each process requires a memory storage of 130 MB. In the present nondimensionalization, $Gr = Re^2$ and $Ra = Re^2 Pr$. The Rayleigh numbers tested are $Ra = 1.0 \times 10^4$, 1.6×10^5, 1.0×10^6, and 1.6×10^7 with unit Prandtl number.

A timing test indicates an average of 1.04 s elapsed wall-clock time is required to complete one BiCGSTAB iteration, 34 s to form and assemble the jacobian matrix and residual

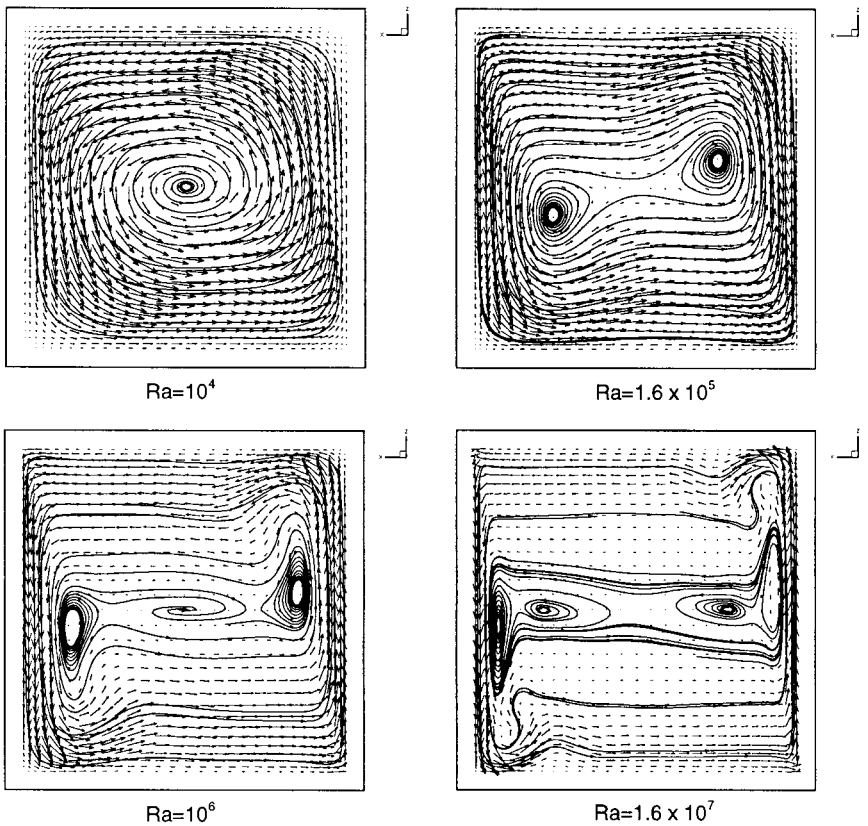

Figure 11. Streamlines for the projected velocity vector field on the symmetry plane $Ra = 10^6$.

vectors for each Newton step. Another 290 s is estimated for the overheads. For $Ra = 10^4$, the computation is started with a zero initial solution field. For the large $\Delta t = 500$, 29 Newton steps and 4361 BiCGSTAB iterations are taken to achieve a solution converged to extremum $\delta Q = 8.5 \times 10^{-6}$. Consequently, a total of 1.62 h was used. The two dimensional planar projection, of the velocity vector field for $Ra = 10^4$ at the symmetry plane reveals only one single recirculation cell (Figure 11).

For $Ra = 1.6 \times 10^5$, the $Ra = 10^4$ solution is used as the initial condition with time step of $\Delta t = 50$. An additional 66 Newton steps and 5106 BiCGSTAB iterations are needed to converge to extremum $\delta Q = 1.9 \times 10^{-5}$. In the symmetry plane, two recirculation cells are now observed, Figure 11.

For $Ra = 10^6$, the previous solution is again used as the initial condition, Δt is reduced to 5. After 195 Newton steps, the steady-state solution is accepted with extremum $\delta Q = 4.7 \times 10^{-5}$. The recirculation cells at the symmetry plane are moving towards the corners, and the isotherms are packing closer to the Dirichlet walls (Figure 12).

For $Ra = 1.6 \times 10^7$, the time step is further reduced to $\Delta t = 0.5$. After 100 time steps with the solution for $Ra = 10^6$ as the initial condition, the extremum iterate is

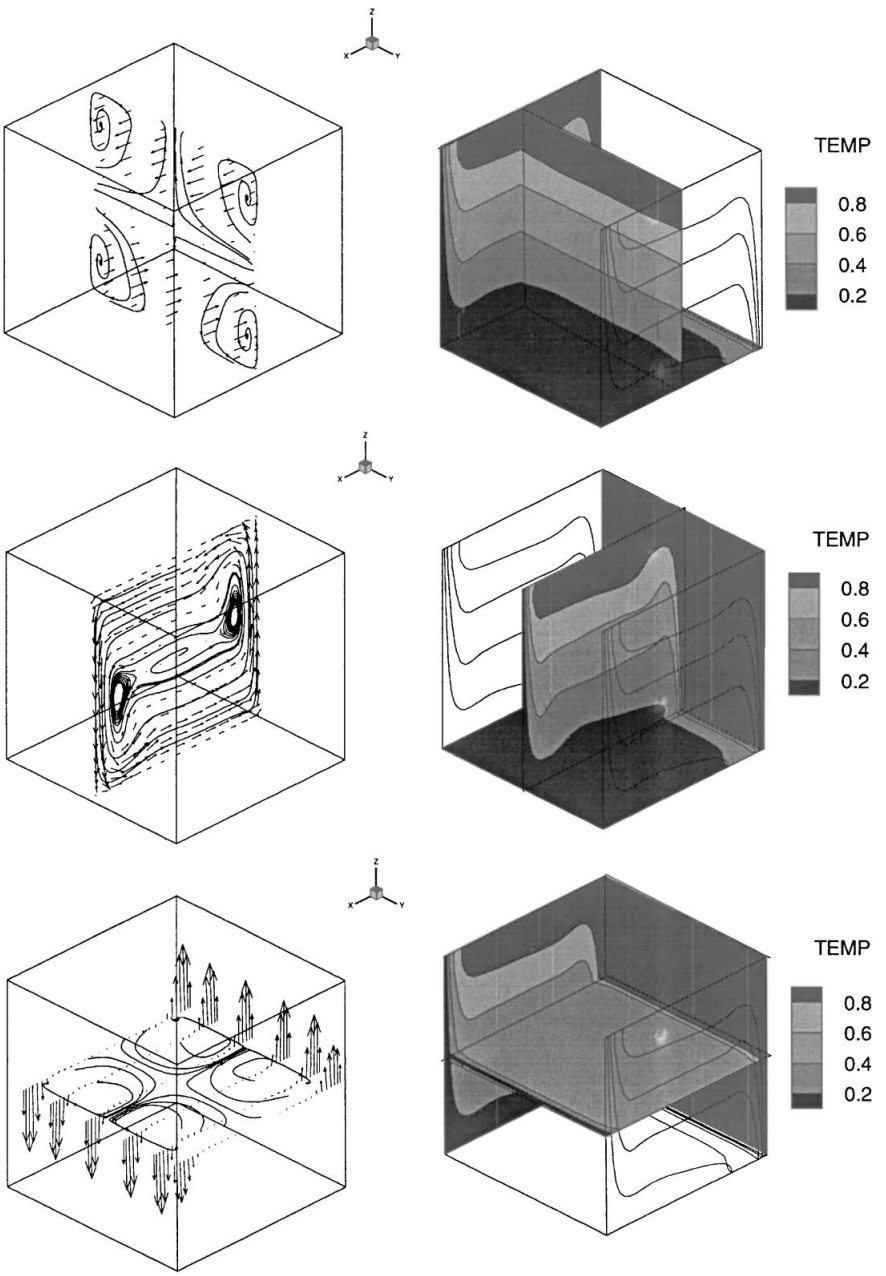

Figure 12. Streamlines for the projected velocity vector field on the symmetry plane $10^4 \leqslant Ra \leqslant 1.6 \times 10^7$.

$\delta Q = 1.7 \times 10^{-3}$ for Ω_y. The effect of the thermal boundary layer to the flow field is obvious (Figure 11). Recirculation cells are further compressed towards the fixed temperature walls.

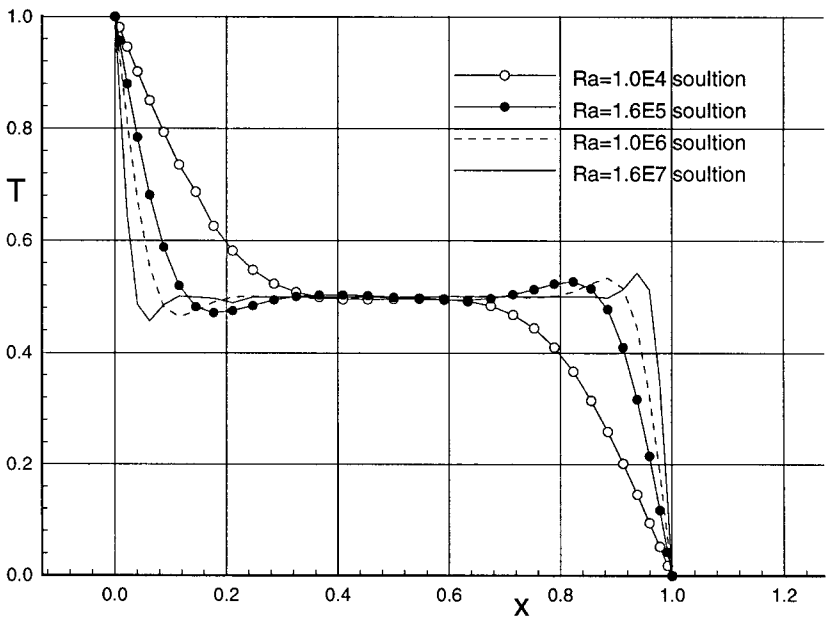

Figure 13. Temperature profiles in the centerline of the symmetry plane for $10^4 \leqslant Ra \leqslant 1.6 \times 10^7$.

The summary streamline plot with projected velocity on the symmetry plane for various Rayleigh numbers is shown in Figure 11. It shares close resemblance to that of the 2D thermal cavity reported by Williams [23].

At large Rayleigh numbers, isotherms with sharp gradients near the walls are observed. The effect of the thermal boundary layer dominates the flow field. Recirculation cells cluster near the walls and move towards the corners. The effect of increasing Rayleigh number of the temperature profile, the u-velocity and the w-velocity components on the symmetry plane are shown in Figures 13 and 14. The temperature profiles at various vertical locations (z-coordinate) on the symmetry plane for $Ra = 10^6$ are shown in Figure 15.

6. CONCLUSIONS

A new parallel finite element CFD algorithm in velocity–vorticity form has been developed for the unsteady, laminar incompressible Navier–Stokes equations in three dimensions. The incompressibility constraint is enforced through a second order kinematic vorticity boundary condition discretization imposed at nodes on all walls. This kinematic vorticity boundary condition enforcement is shown to produce a divergence-free solution.

The fully coupled formulation, which contains seven variables, is solved in parallel on the IBM SP2 computer. The BiCGSTAB sparse iterative solver is incorporated to yield an efficient parallel finite element algorithm. An implicit time integration scheme allows the use of a large time step to achieve a fast steady-state solution for $Re \leqslant 100$. Reducing the size of

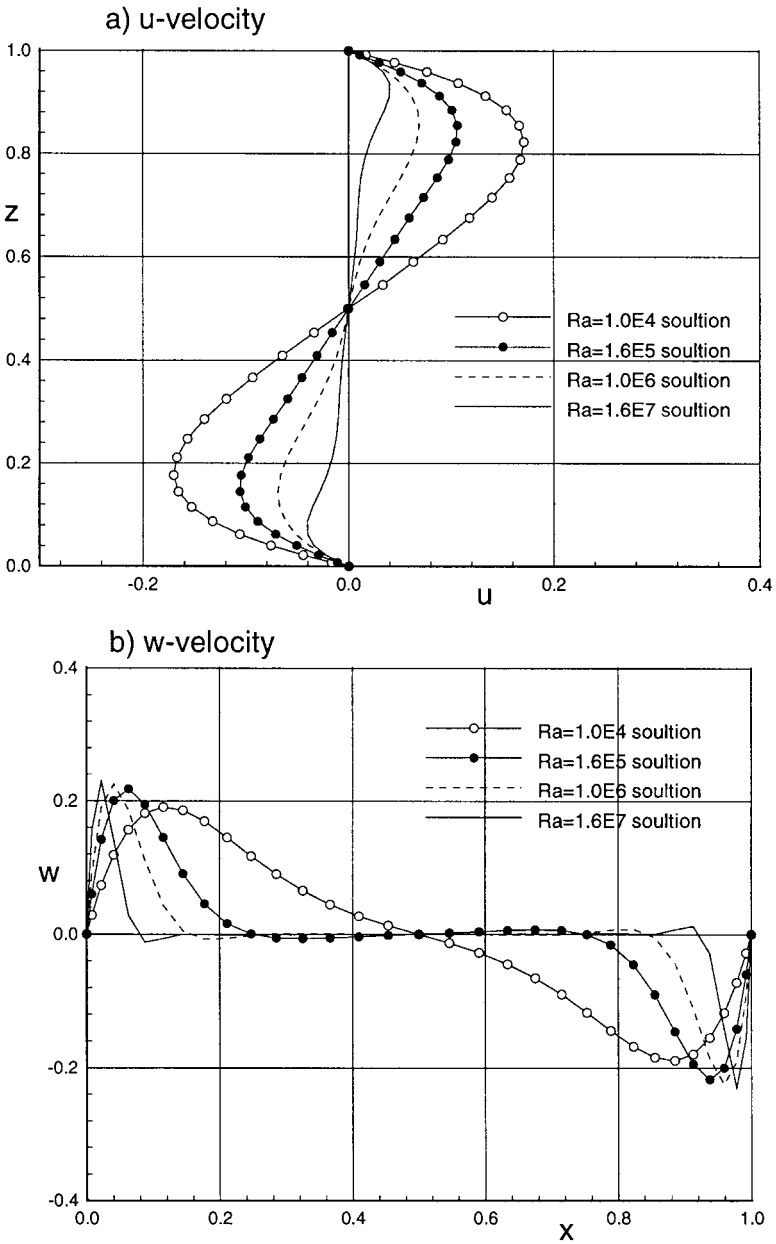

Figure 14. Centerline velocity profiles of the symmetry plane for $10^4 \leqslant Ra \leqslant 1.6 \times 10^7$.

the time step can improve the condition number of the terminal Newton jacobian matrix for large Reynolds number solutions.

The solution-adapted $M = 48 \times 48 \times 48$ mesh produced these reported results, following mesh refinement studies [25]. This mesh density is able to produce solutions of adequate

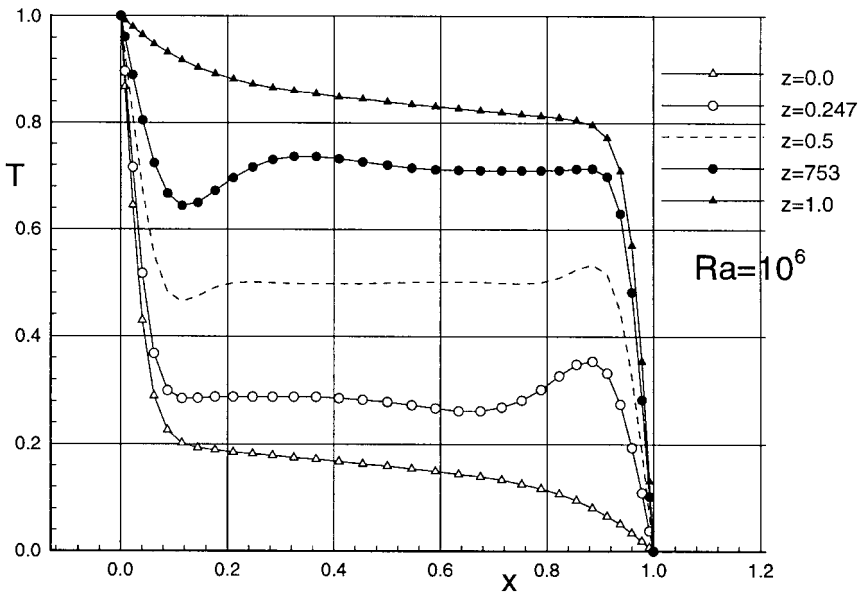

Figure 15. Temperature profile for $Ra = 10^6$ at various z-locations on the symmetry plane.

accuracy for the driven cavity and the thermal cavity benchmarks for the *Re* and *Gr* range selected. The obvious extension of the formulation for the kinematic vorticity condition is to encompass flows in arbitrary geometries. The simplicity of the velocity–vorticity formulation, bearing with the shortfall to solve a fully coupled Newton system, is proven to provide a mathematically viable alternative to a primitive variables, CFD-approximate pressure formulation in a parallel implementation.

REFERENCES

1. Gresho PM, Sani RL. On pressure boundary conditions for the incompressible Navier–Stokes equations. *International Journal for Numerical Methods in Fluids* 1987; **7**:1111–1145.
2. Gresho PM. Some current CFD issues relevant to incompressible Navier–Stokes equations. *Computer Methods in Applied Mechanics and Engineering* 1991; **87**:201–252.
3. Fasel H. Investigation of the stability of boundary layers by a finite-difference model of the Navier–Stokes equations. *Journal of Fluid Mechanics* 1976; **78**:355–383.
4. Orlandi P. Vorticity–velocity formulation for high *Re* flows. *Computers & Fluids* 1987; **15**:137–149.
5. Guj G, Stella F. Numerical solutions of the high-*Re* recirculating flows in vorticity–velocity form. *International Journal for Numerical Methods in Fluids* 1988; **8**:405–416.
6. Daube O. Resolution of the 2D Navier–Stokes equations in velocity–vorticity form by means of an influence matrix technique. *Journal of Computational Physics* 1992; **103**:402–414.
7. Dacles J, Hafez M. Numerical methods for 3-D viscous incompressible flows using velocity–vorticity formulation. *AIAA paper*, AIAA-90-0237.
8. Napolitano M, Pascazio G. A numerical method for the vorticity–velocity Navier–Stokes equations in two and three dimensions. *Computers & Fluids* 1991; **19**:489–495.
9. Guevremont G, Habashi WG, Hafez MM. Finite element solution of the Navier–Stokes equations by a velocity–vorticity method. *International Journal for Numerical Methods in Fluids* 1990; **11**:661–675.
10. Guevremont G, Habashi WG, Kotiuga PL, Hafez MM. Finite element solution of the 3D compressible Navier–Stokes equations by a velocity–vorticity method. *Journal of Computational Physics* 1993; **107**:176–187.

11. Van der Vorst H. Bi-CGSTAB: A fast and smoothly converging variant of Bi-CG for the solution of nonsymmetric linear systems. *SIAM Journal of Science and Statistical Computations* 1992; **13**:631–644.
12. Gunzburger MD, Peterson JS. On finite element approximations of the streamfunction-vorticity and velocity–vorticity equations. *International Journal for Numerical Methods in Fluids* 1988; **8**:1229–1240.
13. Quartapelle L. *Numerical Solution of Incompressible Navier–Stokes Equations*. Birkhauser Verlag: Basel, 1993.
14. Guj G, Stella F. A vorticity–velocity method for numerical solution of 3D incompressible flows. *Journal of Computational Physics* 1993; **106**:286–298.
15. Wong KL. A parallel finite element algorithm for 3D incompressible flow in velocity–vorticity form. Dissertation, The University of Tennessee, August 1995.
16. Barrett R, Berry M, Chan T, Demmel J, Donato J, Dongarra J, Eijkhout V, Pozo R, Romine C, van der Vorst H. *Templates for the Solutions of Linear Systems: Building Blocks for Iterative Methods*. SIAM: Philadelphia, 1994.
17. White Y. *Viscous Fluid Flow*. McGraw-Hill: New York, 1974.
18. Ku HC, Hirsh RS, Taylor TD. A pseudospectral method for solution of the three-dimensional convection diffusion difference schemes. *Journal of Computational Physics* 1987; **70**:439–462.
19. Fujima S, Tabata M, Fukasawa Y. Extension to three dimensional problems of the upwind finite element scheme based on the choice of up- and downwind points. *Computer Methods in Applied Mechanics and Engineering* 1994; **112**:109–132.
20. Babu V, Korpela SA. Numerical solution of the incompressible, three-dimensional Navier–Stokes equations. *Computers & Fluids* 1994; **23**:675–691.
21. Jiang BN, Lin TL, Povinelli LA. Large scale computation of incompressible viscous flows by least-squares finite element method. *Computer Methods in Applied Mechanics and Engineering* 1994; **114**:213–231.
22. Millinson GD, de Vahl Davis G. Three-dimensional natural convection in a box: A numerical study. *Journal of Fluid Mechanics* 1977; **83**:1–31.
23. Williams PT. CCM Continuity Constraint method: A finite-element computational fluid dynamics algorithm for incompressible Navier–Stokes fluid flows. Technical Report, Oak Ridge National Laboratory ORNL/TM-12389, 1993.
24. Fusegi T, Hyun JM. Kuwahara K, Farouk B. A numerical study of three-dimensional natural convection in a differentially heated cubical enclosure. *International Journal of Heat and Mass Transfer* 1991; **34**:1543–1557.
25. Han LS. Hydrodynamics entrance length for incompressible laminar flow in rectangular ducts. *Journal of Applied Mechanics* 1960; **27**:403–409.

